Article

Self-Cleaning Coatings for the Protection of Cementitious Materials: The Effect of Carbon Dot Content on the Enhancement of Catalytic Activity of TiO₂

Charis Gryparis, Themis Krasoudaki and Pagona-Noni Maravelaki *

Laboratory of Materials of Cultural Heritage and Modern Building, School of Architecture,
Technical University of Crete, 73100 Chania, Greece; cgryparis@isc.tuc.gr (C.G.);
themis.krasoudaki@gmail.com (T.K.)
* Correspondence: pmaravelaki@isc.tuc.gr

Abstract: The urgent demand for pollution protection of monuments and buildings forced the interest towards specific preservation methods, such as the application of photocatalytic coatings with self-cleaning and protective activity. TiO₂ photocatalysts without and with a variety of carbon dots loading (TC0, TC25–75) were synthesized via a green, simple, low cost and large-scale hydrothermal method using citric acid, hydroxylamine and titanium isopropoxide (TTIP) and resulted in uniform anatase phase structures. In photocatalysis experiments, TC25 and TC50 composites with 1:3 and 1:1 mass ratio of C-dots solution to TTIP, respectively, showed the best degradation efficiency for methyl orange (MO) under UV-A light, simulated solar light and sunlight compared to TiO₂, commercial Au/TiO₂ (TAu) and catalysts with higher C-dot loading (TC62.5 and TC75). Treatment of cement mortars with a mixture of photocatalyst and a consolidant (FX-C) provided self-cleaning activity under UV-A and visible light. This study produced a variety of new, durable, heavy metal-free C-dots/TiO₂ photocatalysts that operate well under outdoor weather conditions, evidencing the C-dot dosage-dependent performance. For the building protection against pollution, nanostructured photocatalytic films were proposed with consolidation and self-cleaning ability under solar irradiation, deriving from combined protective silica-based agents and TiO₂ photocatalysts free or with low C-dot content.

Keywords: self-cleaning; TiO₂/Cdots; protective films; cultural heritage conservation; photocatalysts; sunlight irradiation

1. Introduction

Air pollution, the fourth greatest fatal health risk so far, is accounting for serious danger to human health, causing millions of premature deaths annually [1]. There is a demanding need to combat climate change as far as the global population grows; thus, highly efficient technologies can serve as the key to improving air quality and protecting the environment [2,3]. Moreover, air pollution and climate change cause physical and aesthetic damage to buildings and cultural heritage constructions, accelerating the decay process [4]. For the protective treatment of several types of building substrates, advanced coatings with self-cleaning ability have been developed throughout the years [5]. The main advantage of photocatalytic air and wastewater purification is that chemicals or external energy input are not requisite, except for ambient light or sunlight, which is not costly. Despite the strong effort for the development of various novel active materials, titanium dioxide (TiO₂) is by far the most promising and widely employed technology in photocatalysis among them [6].

TiO₂ was introduced in the field of photocatalysis in 1972 [7], and since then, it has become the most investigated compound for air purification due to its excellent physico-chemical stability and oxidation properties, as well as cost-effectiveness, high availability and eco-friendliness [8]. Photoinduced processes begin with the absorption of electromag-

netic radiation (UV-light) by TiO_2, which cause an electron to be promoted from the valence band (VB) to the conduction band (CB), leaving a positively charged hole in the VB [9]:

$$TiO_2 + h\nu \rightarrow e^-_{CB} + h^+_{VB} \tag{1}$$

introducing the energy gap (Eg), one of the most useful characteristics in semiconductor field (Equation (1)). Afterward, electron and hole separately may take part in reduction and oxidation reactions, respectively, with species such as H_2O, O_2 and OH^- adsorbed on the TiO_2 surface. These species can be oxidized to OH radical or reduced to $O_2\bullet$, which can react with the pollutant, leading to decomposition of the latter. Since the ideal photocatalyst offers a combination of low Eg and efficient charge separation, TiO_2, when solely used, has limited performance in outdoor conditions. TiO_2 appears in three crystalline phases: rutile and anatase are both tetragonal, and brookite is orthorhombic [10]. Although anatase has a larger bandgap (3.2 eV) compared to rutile and brookite (3.0 eV), its photocatalytic activity is apparently superior to that of rutile, while synthesis of pure brookite is a demanding challenge. Most research is focused on anatase due to the high surface adsorption capacity and the indirect bandgap, which leads to a much longer lifetime of photogenerated holes and electrons compared to the larger grain size and direct bandgap of rutile [11]. Even in the form of anatase, the bandgap of TiO_2 can be approached by UV light irradiation ($\lambda \leq 380$ nm, 5% of sunlight), but the low photoenergy of visible light is not sufficient for the excitation of electrons. Thus, in order to increase the photocatalytic activity and take advantage of solar light, modified TiO_2 photocatalysts, such as TiO_2 loaded with Carbon Dots (TiO_2/C-dots, TC), is necessary.

C-dots, byproducts of carbon nanotubes purification accidentally isolated in 2004 [12], have attracted intense attention in photocatalytic applications due to their low toxicity, good photostability, small size and low synthetic cost even on a large scale [13]. Moreover, their strong and tunable photoluminescence enables their application in biomedicine, optoelectronic devices and biosensing [14]. A typical C-dot is a small carbon nanoparticle functionalized on its surface by organic molecules, typically acids or amines, using various chemical reactions. This functionalization plays an important role in the characteristic properties of C-dots due to the defects of the organic groups on the surface of each C-dot, which can cause efficient charge separation, leading to radiative recombination of holes and electrons with subsequent fluorescence emission [15].

There are several reports regarding the synthesis of C-dots, or nitrogen-doped C-dots, and TiO_2 nanocomposites with applications in the photocatalytic degradation of organic dyes [16–25]. The synthetic process of these methodologies required either prolonged heating time for C-dots preparation [16,17] or calcination at 400–500 °C [18,19] and even at 700 °C [20] in the TiO_2/C-dots' step of the synthesis. In another study, a one-step solvothermal route was proposed, showing remarkable photocatalytic degradation of methylene blue (MB) under UV light [21]. However, for the successful degradation of methyl orange (MO) and Rhodamine B (RB) under UV, calcination of catalyst at 400 °C was inevitable. Other studies used specialized equipment, such as high-pressure Teflon-lined sealed autoclave containers [22,23] or a combination with spin coating method [24] for the controlled synthesis of C-dots, making large-scale production prohibitive. Finally, in all cases, the cycling performance of the synthesized photocatalysts exhibited moderate degradation ($\leq$70% after six cycles) [23,25].

Recently, we developed an efficient, simple and low-cost method for the synthesis of pure TiO_2 and TiO_2/C-dots and studied comparatively into the photodegradation of MO under UV-A and visible light, with promising results [26]. MO was used as a model compound because it is a common, highly toxic dye that exhibits good photostability upon light irradiation under different conditions [27] and resistance to complete biodegradation. In this study, using a similar methodology, five TiO_2-based compounds were synthesized containing different C-dot loading, namely TC0, TC25, TC50, TC62.5 and TC75, and analyzed by several techniques, such as X-Ray diffraction (XRD), scanning and transmission electron microscopies (SEM, TEM) and UV-Vis/near-IR diffuse reflectance. These TiO_2/C-

dots nanocomposites were used as model photocatalysts to investigate the effect of the C-dot content in photocatalytic degradation of MO under UV-A and visible light, but also direct sunlight radiation, showing remarkable results compared to pure TiO_2 (TC0), as well as commercially available Au/TiO_2 (TAu) and this is the first innovative result of this study. The most suitable photocatalysts were found to be TC25 and TC50, evidencing that this range of C-dot loading is superior for the decomposition of organic pollutants, another interesting finding that correlates Cdots amount and efficiency. Another innovation of this study, apart from the rapid and excellent photocatalytic activity of these catalysts under solar light irradiation, is the almost eternal nature, as they can be recycled and reused up to ten times without losing their catalytic ability (~90% degradation after 3 h of irradiation into the 10th cycle, >99% after 6 h).

Furthermore, based on the tetraethoxysilane (TEOS) effectiveness as a strengthening agent for Portland cement mortars [28], we synthesized an advanced hydrophobic consolidant, designated as FX-C, using a sol–gel process that combines TEOS, PDMS and nano-calcium oxalate (nano-CaOx) for the preservation of cultural heritage [29,30]. It was found that silicon in TEOS/PDMS copolymer can form strong Si–O bonds with hydroxyl groups of the material for preservation [31]. It is well-established that among other useful properties of TiO_2-based catalysts [32–34], coating application of nano-TiO_2 or $SiO_2@TiO_2$ [35–38] in mortars provides restoration and self-cleaning ability in building materials [39–41], while TEOS-PDMS-TiO_2 hybrid nanomaterials in limestone and marbles enhance these properties [42,43]. Our previous work that studied the self-cleaning ability of the composite coating FX-C with TiO_2/C-dots in concrete, limestones and lime mortars showed a moderate photocatalytic activity of this protective agent under visible light irradiation [26]. The fourth innovative result of this work refers to the accomplishment of a self-cleaning coating of FX-C and TC0–TC25 activated under visible light irradiation, ready to be applied onto cementitious mortars.

2. Materials and Methods

2.1. Materials

The citric acid (monohydrate, ≥99%) and hydroxylamine hydrochloride (99%) were employed from Sigma-Aldrich (St. Louis, MI, USA) as C-dots precursors and used as received. Titanium (IV) isopropoxide (TTIP, ≥97%) and hydrochloric acid (~37%) were purchased from Sigma-Aldrich (St Louis, MI, USA) and used as received for the synthesis of TC0–75 powders. Methyl Orange (for microscopy, Hist.) was obtained from Sigma Aldrich (St Louis, MI, USA) and utilized as the model compound for the degradation of organic pollutants. Gold 1% on titanium dioxide extrudates was employed from Strem Chemicals (Newburyport, MA, USA) and used as received. Commercially available solvents were used as received without further purification.

2.2. Analytical Techniques

High-resolution TEM micrographs of C-dots and TC0–75 were obtained using a JEM-2100 transmission electron microscope and a JEM-100C microscope (JEOL Ltd., Tokyo, Japan), operating at an accelerating voltage of 200 kV and 80 kV, respectively. The samples for TEM were prepared by drop-casting 8 μL of the diluted aqueous solution of each sample onto Formvar/carbon–copper-coated grids supplied by Agar Scientific (Essex, UK) and then left to dry at room temperature for 2 h. A transmission electron microscope was also used for statistical size-distribution histograms by counting and measuring the diameter size distribution via ImageJ software. SEM images were recorded on a JSM 6390LV scanning electron microscope (JEOL Ltd., Tokyo, Japan) operated at 20 kV electron voltage. TC nanoparticles were dried on a two-sided carbon tape and sputter-coated with ca. 100 Å of gold (Au), using an SCD 050 sputter coater (BAL-TEC, Los Angeles, CA, USA). UV-Vis spectra of samples were obtained on a Cary 1E UV-Vis spectrophotometer (Varian, Palo Alto, CA, USA), in the wavelength range between 200 and 700 nm, using a quartz cuvette with 10 mm path length and 3.5 mL chamber volume. UV-Vis/near-IR diffuse

reflectance spectra were recorded on a UV-2600 spectrophotometer (Shimadzu, Kyoto, Japan) using $BaSO_4$ as the 100% reflectance reference. Powder X-ray diffraction data (XRD) of the TC0–75 catalysts were obtained from a D8 Advance X-ray diffractometer (Bruker, Billerica, MA, USA) equipped with a Lynx Eye strip silicon detector (Bruker, Billerica, MA, USA). Measurements were applied at room temperature, using Cu Ka radiation at 35 mA and 35 kV. Fourier Transform Infrared spectroscopy (FT-IR) in powdered samples was performed with an iS50 FT-IR spectrometer (Thermo Fischer Scientific, Waltham, MA, USA) in the spectral range between 4000 and 400 cm^{-1}. For Attenuated Total Reflection (ATR) measurements, a built-in, all-reflective diamond was used as the internal reflection element. The measurement of the color change via photocatalytic degradation was performed with a CM-2600d spectrophotometer (Konica Minolta, Tokyo, Japan) with a D65 illuminant at 8-degree viewing, in the wavelength range between 360 and 740 nm. A 36 W UV EBN001W LED curing lamp (340–380 nm, maximum emission at 365 nm, Esperanza sp. j. Poterek, Ożarów Mazowiecki, Poland) provided the UV-A irradiation source, while a laboratory constructed stimulated solar box equipped with two L15W/840 tubular fluorescent lamps (400–630 nm, maximum emission at 540 nm, OSRAM, Munich, Germany) was used as the solar simulator. A GM3120 (BENETECH, Shenzhen, China) electromagnetic radiation tester was used to measure light irradiance.

2.3. Synthesis of Carbon Dots

Regarding the C-dots preparation, the procedure was slightly modified from an already published process [44]. A solution of citric acid (1.65 g) and hydroxylamine hydrochloride (1.65 g) in deionized water (16.5 mL) was heated at 300 °C for 12 min. The resulting dark brown, sticky solid was dissolved in water, sonicated via ultrasonic agitation for 10 min to separate the aggregates and filtered through a 7–12 μm Whatman filter paper to remove undissolved byproducts. A final 2.5% *w/v* C-dots solution was collected as an opaque liquid (Figure 1).
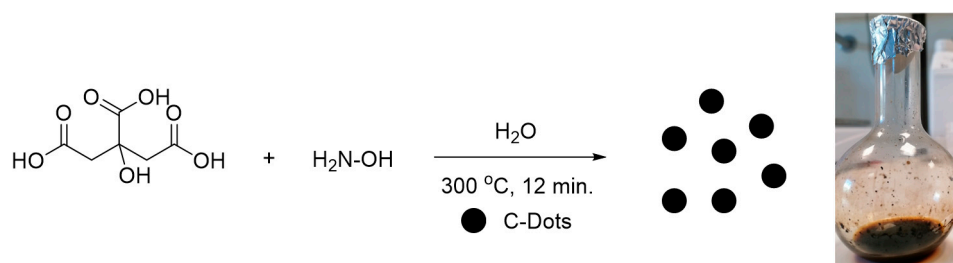

Figure 1. Hydrothermal synthesis of C-Dots.

2.4. Synthesis of TiO_2 (TC0) and TC25–75 Photocatalysts

For the preparation of TiO_2 with different loading of C-dots, an already published method was followed [26], employing slight modifications (Figure 2). Briefly, a 2.5% *w/v* aqueous C-dots solution, specifically 1.5 g for TC25 up to 13.5 g for TC75, was dissolved in a 1:1 mixture of ethanol and deionized water (50 mL). For this solution, a solution of TTIP (4.5 g) in ethanol (20 mL) was added dropwise, and the pH of the resulting mixture was adjusted to 2.5 by the addition of concentrated HCl (~5 drops) to facilitate the hydrolysis of TTIP. The mixture was allowed to stir at ambient temperature overnight, followed by heating at 80 °C for 8 h to facilitate titania polymerization and C-dots incorporation. Afterward, the mixture was cooled to ambient temperature, centrifuged for 10 min at 3000 rpm, and the wet solid was dried at 80 °C and ground using a mortar. Finally, the catalyst was calcinated at 200 °C for 2 h to produce the crystalline material as a yellow (TC25) to brown solid (TC50–75) in 85%–98% yield.
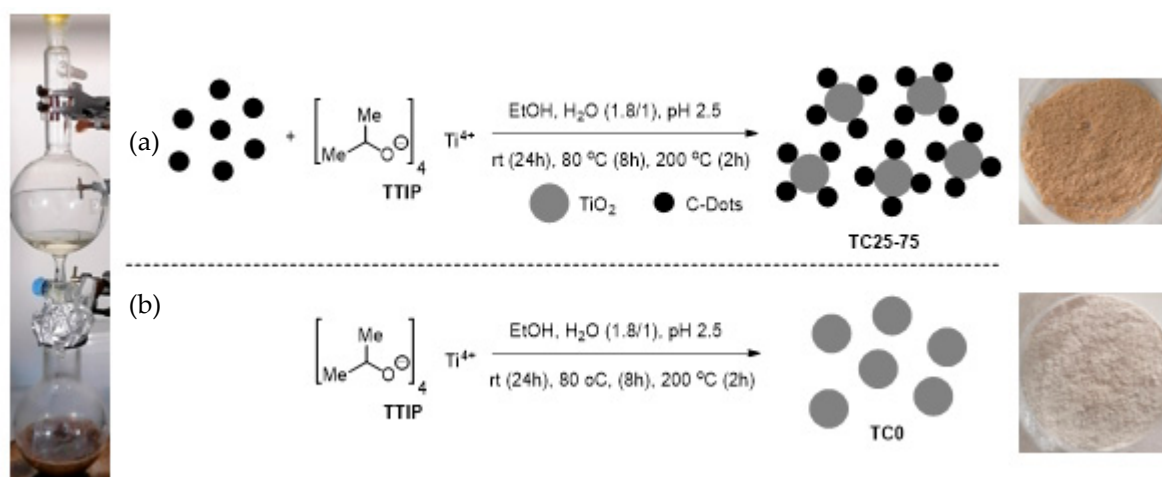
Figure 2. Synthesis of (**a**) TiO$_2$ enriched with C-dots (TC25–75) and (**b**) TiO$_2$ (TC0).

The same process, in the absence of the aqueous C-dots solution, was applied for the synthesis of TiO$_2$ as a control substance (Figure 2). It is worth mentioning that a crucial factor in this experiment is the adjustment of pH at 2.5 since lower pH leads to a reduction in the isolated yield of the catalyst. For example, at pH 1.5, the isolated yield of TC50 drops to 46%. Furthermore, in the process of synthesis of the control substance TC0, acidification up to pH 1.5 leads to a mixture of brookite and anatase phases of TiO$_2$, whereas at pH 2.5, only the anatase phase is present, as indicated in the XRD analysis.

2.5. Incorporation of Photocatalysts into the Protective Agent

Consolidant FX-C was prepared in the laboratory by an already published method [29]. Each solid catalyst (4% w/w) was added to the sol FX-C, and the mixture was sonicated via ultrasonic agitation for 10 min to ensure homogeneity (Figure S1).

2.6. Application of the Protective/Photocatalytic Film onto Cementitious Mortars

The performance of the photocatalytic films in the conservation of cement-based materials was evaluated using cement mortars prepared in the laboratory, with a binder/sand ratio of 1:3, based on local 0–3 mm of grain size standard sand of carbonaceous nature. Further information on the mix design of the treated mortars can be found in Table S1. The synthesized photocatalytic films were brushed three times on the cement mortar substrates. Control experiments were also performed by measuring the untreated cement mortar and by brushing the cementitious material with FX-C in the absence of a photocatalyst.

2.7. Photodegradation of MO Using Photocatalysts and Their Reusability

The activity of a series of TC nanocomposites on the photodegradation of MO was initially evaluated under UV-A light, using a 36 W LED curing lamp (maximum emission at 365 nm) with a light irradiance of approximately 33.6 mW/cm^2 and artificial solar light, using a solar box equipped with two 15 W tubular fluorescent lamps (maximum emission at 540 nm) with a light irradiance of approximately 13.6 mW/cm^2. For both irradiation types, the distance of each sample from the lamps was set to 7 cm.

The photocatalytic activity of TC25, TC50, TC62.5 and TC75 catalysts, compared to TC0, was evaluated by studying the photodegradation of MO solution in the presence of the appropriate catalyst under UV-A light, simulated solar light, as well as sunlight in outdoor weather conditions. For this purpose, the solid photocatalyst (40 mg, 0.08% w/v) was dispersed to a 5 ppm MO aqueous solution (50 mL), and the mixture was allowed to stir in darkness for 30 min in order to reach adsorption–desorption equilibrium of dye on the catalyst surface. Thereafter, the mixture was irradiated with the appropriate light source for a period of 120 min, with a sample removal (4 mL) every 15 min for reaction monitoring. Analytical determination of the reduction in MO concentration during the

photocatalytic degradation process was carried out spectrophotometrically at 465 nm. A commercially available catalyst Au (1%)/TiO_2 (TAu) was also used in the MO degradation under sunlight conditions for comparison. Under the same conditions, MO degradation was tested in the absence of a catalyst, where no decomposition was observed.

Furthermore, the reusability of TC50 was tested under simulated sunlight irradiation. In this case, TC50 (0.16 g) was added into a 5 ppm aqueous MO solution (80 mL) and irradiated with visible light for 180 min. After each cycle, the solution was decanted, and the catalyst was washed with water and ethanol (30 mL each), dried at 60 °C overnight, and then reused in the next cycle. This process was repeated 9 times, while at the end of the 10th cycle, the catalyst was recycled (0.08 g) and could be further used in the next experiment.

2.8. Self-Cleaning Performance of Treated Cementitious Mortars

In order to determine the self-cleaning and air depolluting capabilities of the protective films enhanced with TiO_2/C-dots, the protective coating was brushed onto the cement mortar substrates, and the photodegradation of a drop of MB under UV-A and visible light was determined using a portable CM-2600d spectrophotometer (Konica Minolta, Tokyo, Japan). Control experiments were performed by exposing the untreated cement mortar and the cementitious material with FX-C, covered with the same amount of MB. The total color difference (ΔE) can be calculated using the following equation [45]:

$$\Delta E = \sqrt{\Delta L^{*2} + \Delta a^{*2} + \Delta b^{*2}} \qquad (2)$$

where the differences in color (Δ) with time, for the treated with a protective coating and spotted with MB cement mortars, were expressed as *L**, *a** and *b** values of the CIELab color space. The *L** values range from 0 for black to +100 for white, while the negative and positive *a** values represent green and red, respectively. As for the negative and positive *b** values, these represent blue and yellow, respectively.

3. Results and Discussion

3.1. Structure and Morphology of C-Dots and TC0-75 Photocatalysts

Figure 3 illustrates the XRD patterns of the pure synthesized TiO_2 (TC0) and TC25–75, evidencing the crystalline phases present in the samples.
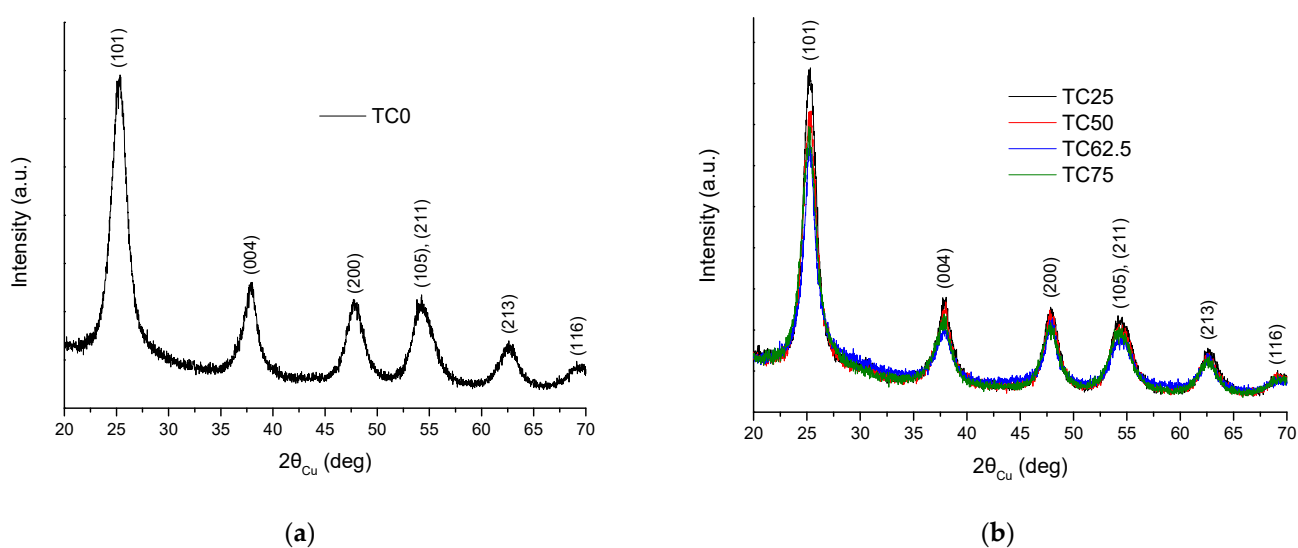

(a)

(b)

Figure 3. X-ray diffraction patterns of (**a**) TiO_2 (TC0) and (**b**) TiO_2 with different C-dot loading (TC25–75).

The diffractograms reveal the formation of anatase phase (JCPDS card no. 00-021-1272) exclusively in all the synthesized materials, excluding other possible phases of titania, such

as rutile or brookite. The anatase crystalline phase is commonly accepted as a more efficient photocatalyst, compared to rutile and brookite, due to its high photocatalytic activity [46]. Crystallite average size of the TC0–75 nanoparticles was estimated using the following Scherrer equation [47]:

$$D = \frac{K\lambda}{\beta\ \cos\theta} \tag{3}$$

where D is the crystallite particle size (in nm), K is the Scherrer constant equal to ~0.9 in the case of spherical shapes, λ is the wavelength of the X-ray's radiation (0.15406 nm), β is the full width at half maximum (FWHM) height of the diffraction peaks and θ is the Bragg's diffraction angle. The diffraction peaks at 25.2°, 37.9°, 47.9° and 62.7° correspond to phases (101), (004), (200) and (213), respectively, while the peak appearing at 2θ 54.3° is attributed to both (105) and (211) phases. The crystallite size of the photocatalysts was calculated using the (101) peak and found to be 4.53, 6.06, 5,36, 6.35 and 5.07 nm for samples TC0, TC25, TC50, TC62.5 and TC75, respectively, showing only a slight increase in crystallite size with C-dot incorporation. The results are in good agreement with previous findings, showing the correlation between the low calcination temperature and the small crystal size of TiO_2 [48–50], as well as the stability of anatase when the particle size is below 14 nm [51].

TEM images of the as-synthesized C-dots (Figure S3) were similar to that observed in our previous work [26]. The average size of C-dots was 1.9 nm, ranging from 1.2 to 2.6 nm, and the shape appeared to be uniform and quasi-spherical (Figure S3c). TEM analysis of the TC50 and TC75 photocatalysts can be seen in Figure 4a,b. TC50 exhibited relatively uniform size nanoparticles, with an average size of 20–21 nm and the size distribution ranging approximately from 14 to 32 nm. In a previous work, a similar size distribution ranging from 10 to 40 nm for the TC25 photocatalyst was observed [26]. Agglomeration of crystallites resulting in nanocluster formation was observed in previous works for TiO_2 [52,53] and TiO_2 doped with C-dots [10] or with other species [54,55]. TEM images of TC75 nanoparticles in Figure 4c,d show a non-uniform but quasi-spherical shape in an average size of 64–68 nm and wide size distribution of 40 to 100 nm (Figure S4) due to the high C-dot loading in the TiO_2 surface. The XRD results and the crystal planes observed in the TEM images of our previous work for TC25 [26] were both attributed to the crystalline structure of the TiO_2/C-dots nanoparticles, further evidenced in the SEM images in Figure 4. Even though the synthesis of pure anatase requires calcinations at 500 °C within several hours [56], nevertheless, in our case, TEM images indicated that at a relatively low temperature, a C-dots-assisted crystalline TiO_2 could be formed [26].

Indeed, SEM was used to display the surface morphology of TC25 and TC62.5 nanocomposites (Figure 5). Both nanohybrids consist of nearly spherical in shape, rough and compact aggregates with crystal structures and various diameters. The spherical-like shape is typical for anatase crystallite structure [10].

The mineralogical and microstructural characterization of the studied photocatalysts revealed that anatase was formed in the presence of different C-dot loading upon a heating process up to 200 °C. By increasing the C-dot loading, as in the case of the TC75, the average size of the photocatalysts was also increased due to agglomeration phenomena.

The FTIR spectrum of C-dots (Figure 6) confirms the presence of polar groups derived from the incorporation of hydroxylamine into the carbon core. This observation is in accordance with the good dispersion properties that C-dots exhibit in water. More specifically, the broad peaks at 3450 and 3200 cm^{-1} correspond to the symmetric stretching vibration of O–H and N–H, respectively [23], while the peaks at 1605 and 1399 cm^{-1} can be attributed to the asymmetric and symmetric stretching vibration of COO^- [57]. The stretching vibration of C=O at 1697 cm^{-1} along with the bending vibration of N–H in amides at 1584 cm^{-1} [26,58] and the stretching vibration of C-O in carboxylates at 1183 cm^{-1} are also present in the C-dots spectrum. Other characteristic peaks of the main core in carbon dots can be considered: (a) the asymmetric and symmetric stretching vibration of C–H bonds with the broad peaks at 3041 and 2807 cm^{-1}, and (b) the stretching and bending vibrations of C=C at 1630 and 746 cm^{-1}. Finally, it is important to highlight that in the FTIR spectra

of the TC25–75 photocatalysts (Figure 6), characteristic bands of C-dots at 1698, 1605 and 1183 cm^{-1} were shifted to higher and lower wavenumbers (e.g., 1630, 1552 and 1223 cm^{-1}, respectively), due to the C-dots' incorporation in the TiO$_2$ surface. In the sample TC75, the higher intensity of the C–H asymmetric and symmetric stretching vibrations at 2921 and 2852 cm^{-1} is directly correlated with the higher C-dots content.
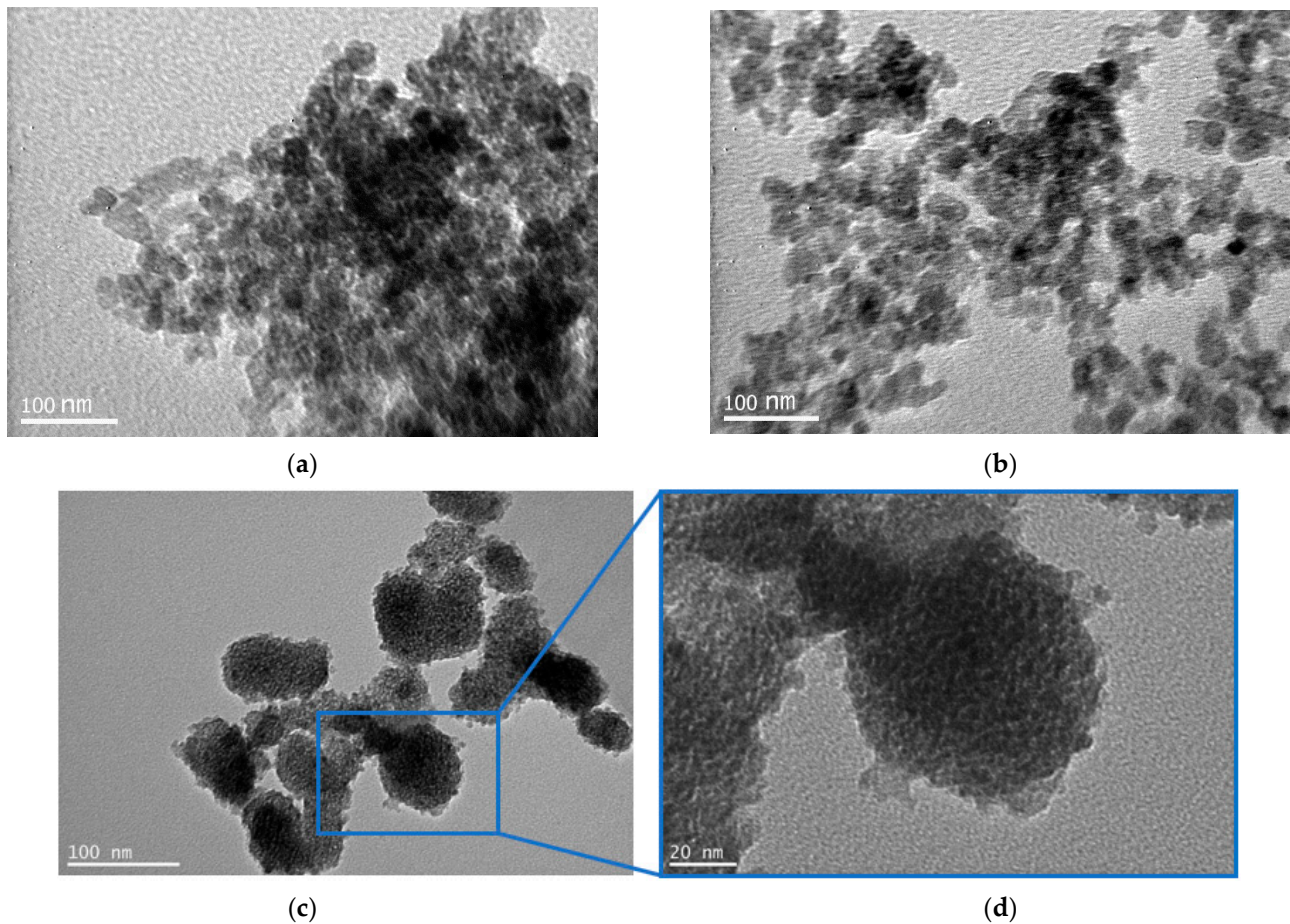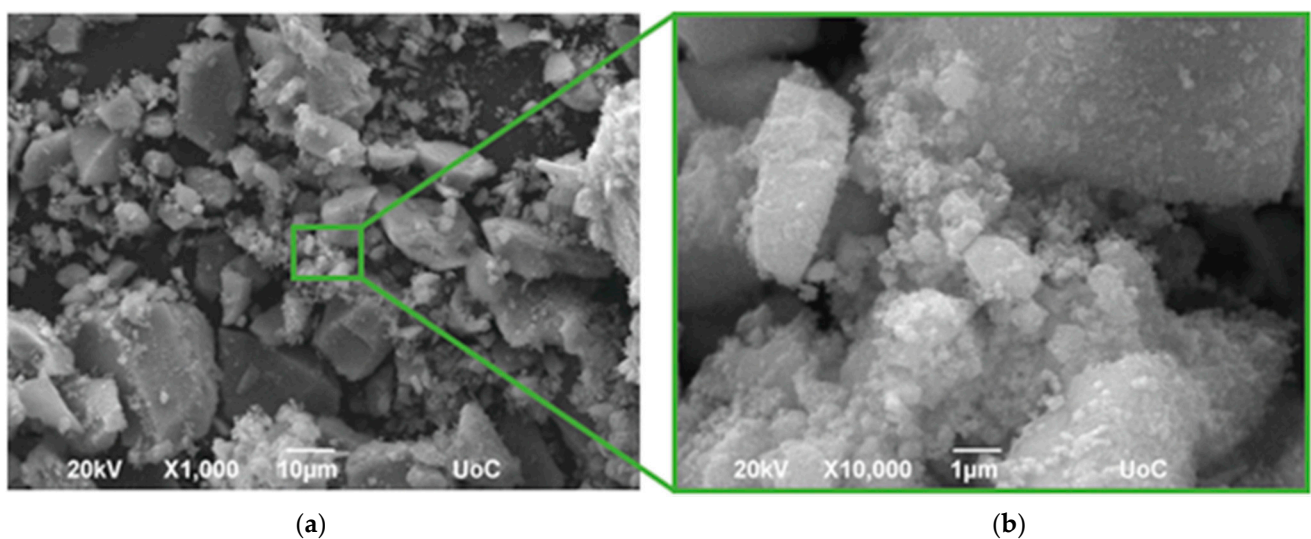

Figure 4. TEM images of (**a**,**b**) TC50 and (**c**,**d**) TC75 nanocomposites.
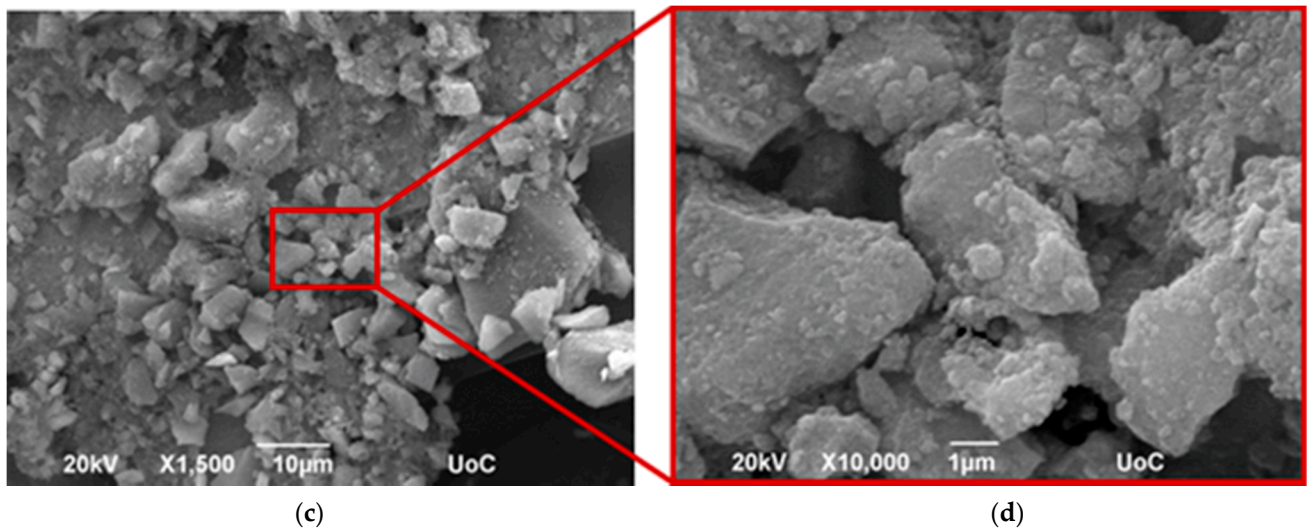

Figure 5. *Cont.*

(c)　　　　　　　　　　　　　(d)

Figure 5. SEM images of (**a**,**b**) TC25 and (**c**,**d**) TC62.5 nanocomposites.

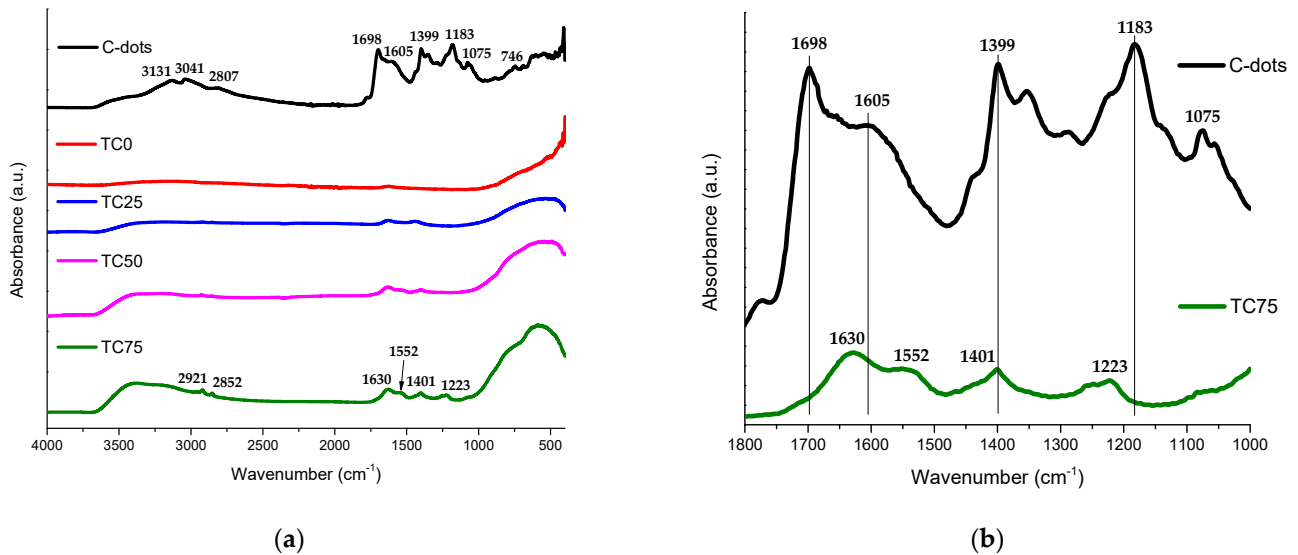
(**a**)　　　　　　　　　　　　　(**b**)

Figure 6. FTIR spectra of (**a**) C-dots, TC0, TC25, TC50 and TC75 photocatalysts and (**b**) the zoom area (1800–1000 cm^{-1}) of C-dots and TC75 photocatalyst.

The optical properties of the TC0–75 photocatalysts were studied by UV-Vis/NIR diffuse reflectance spectroscopic (DRS) measurement (Figure 7a). It is obvious that the absorption edge of TC25–75 was shifted towards the visible light region compared to TC0, suggesting significant absorption ability for solar light. The energy band gaps (Eg) of photocatalysts TC0–75 were determined from UV-Vis/NIR diffuse reflectance spectra (Figure 7b), using Tauc plot analysis for indirect allowed transition [59], due to the anatase crystallite form of TC structures. In this case, $(f\ hv)^{1/2}$ is expressed as a function of photon energy (hv), where f is the Kubelka–Munk function [60] of the measured reflectance (R), as shown in the following equation:
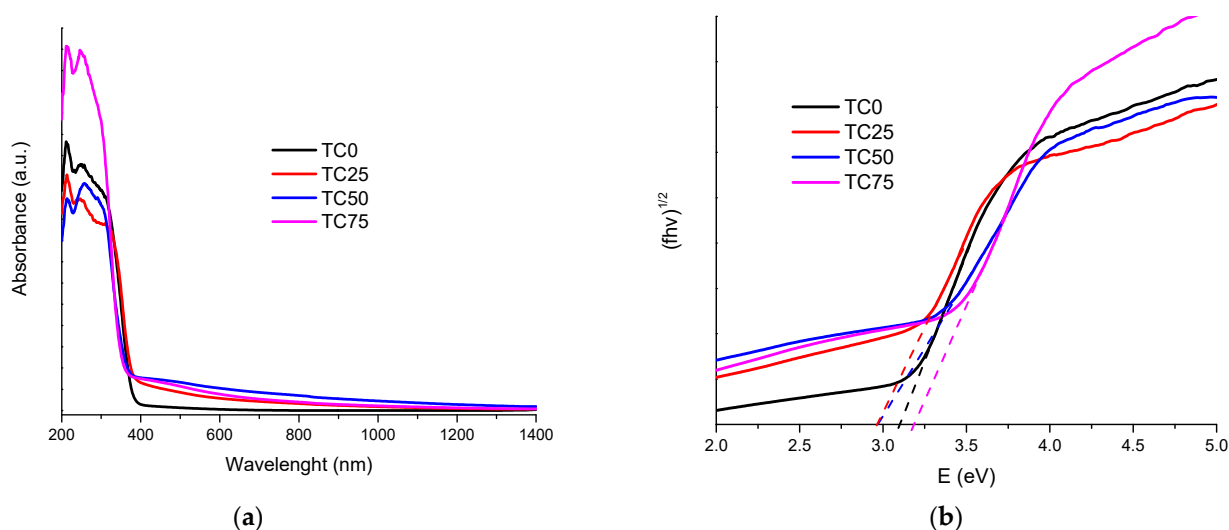
$$f(R) = \frac{(1-R)^2}{2R} \tag{4}$$

Figure 7. (**a**) UV-Vis/NIR diffuse reflectance spectra and (**b**) Tauc plots for TiO$_2$ (TC0), TC25, TC50 and TC75 photocatalysts.

This analysis led to Eg values of 3.10 eV for TC0, which is close to the bandgap of anatase. On the contrary, the bandgaps of TC25 and TC50 were measured at 2.97 eV each, while TC75 exhibited a bandgap of 3.18 eV. The findings are in correlation with the photocatalysis results, suggesting that the Eg of the nanocomposites appears to be an important parameter that accounts for the efficiency of the photocatalytic process. Thus, C-dots can reduce the energy bandgap of TiO$_2$ up to a point where C-dots dominate the structure of the photocatalyst, leading to an even higher Eg than TiO$_2$, as in the case of TC75 with higher C-dot content.

3.2. Photocatalytic Performance of TC25–75 Compared to TCO and TAu

The results of the UV-A irradiation process were shown in Figure 8a, where TC25–62.5 composites provided a much higher photodegradation rate for MO compared to TiO$_2$ (TC0) and TC75, with both TC25 and TC50 photocatalysts showing the best performance. The light irradiance of the 36 W LED curing lamp used in our experiments, based on the sample distance, was approximately 33.6 mW/cm^2. The area of a 50 mL beaker that was used in the experiments can be defined as half the curved surface area of the cylinder, πrh, where r is the base radius, and h is the height of the cylinder. Therefore, the average continual radiation was ~1.42 W. After 60 min of UV-A light irradiation, the MO degradation rates in the presence of TC0, TC25, TC50, TC62.5 and TC75 were 20.8, 91.4, 92.0, 56.9 and 48.7%, respectively. C-dots had almost no photocatalytic ability for MO, as only a 4.6% of the dye was degraded after 60 min. The UV-Vis spectrum and macroscopic evaluation of MO degradation using TC50 under UV-A light are displayed in Figures S5 and S6. Similar results, in a slower degradation rate, were found during the simulated solar light irradiation, as shown in Figure 8b. The light irradiance of the two 15 W fluorescent lamps, based on the sample distance, was measured at 13.6 mW/cm^2; thus, the average continual radiation was ~0.58 W. It is evident that all of the TC25–75 composites exhibited higher photocatalytic activity for MO compared to TC0, whereas both TC25 and TC50 provided the highest degradation rate. More specifically, after 120 min of irradiation, the MO degradation rates in the presence of TC0, TC25, TC50, TC62 and TC75 were 45.4, 96.2, 90.9, 62.9 and 46.1%, respectively. The UV-Vis spectrum and macroscopic evaluation of MO degradation using TC50 under visible light are reported in Figures S7 and S8.
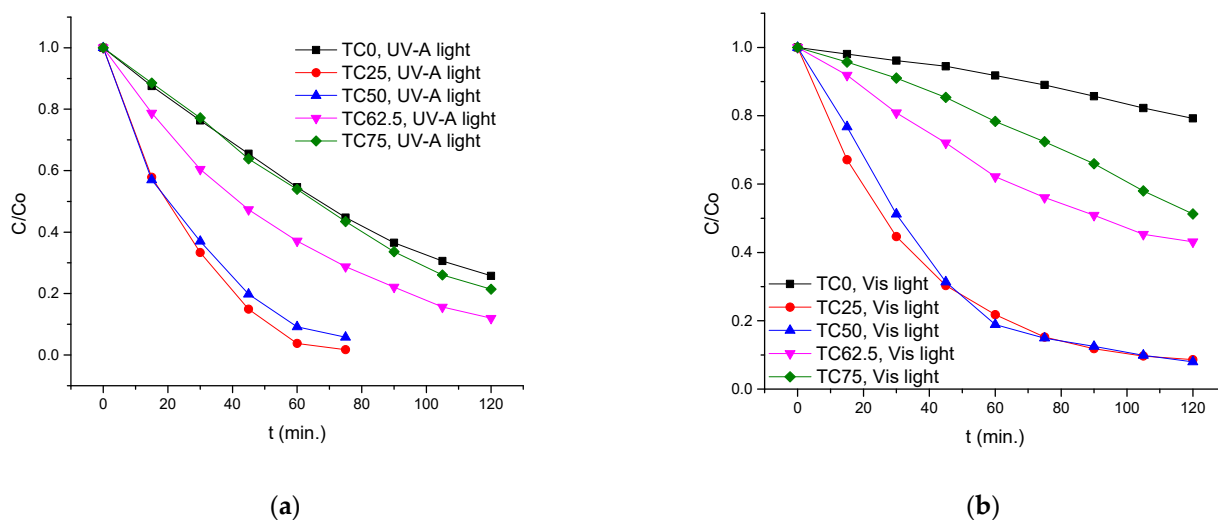
Figure 8. MO degradation rates in the presence of TC0–75 photocatalysts under (**a**) UV-A and (**b**) simulated solar irradiation.

In all photocatalytic experiments, the concentration of MO was fixed at 5 ppm. It is worth mentioning that for concentrations ranging from 5 to 25 ppm, the highest photocatalytic activity was found to be 20 ppm in an anatase titania suspension system, with 5 ppm being the least suitable MO concentration [61]. MO exhibits the lowest degradation rate compared to RhB and MB because an electron is more difficult to be transferred to TiO_2, as the Highest Occupied Molecular Orbital (HOMO) energy gap of MO is -5.624 eV, compared to -10.128 eV for RhB and -10.494 for MB [62]. For those reasons, the high photocatalytic activity of nanocomposites TC25 and TC50 in MO degradation can be described as a remarkable result.

Furthermore, the same photocatalytic group of TC nanocomposites was tested on the photodegradation of MO under solar light in outdoor weather conditions. According to accurate weather station data [63], during the days that the experiments took place in our department area, the daily all-sky surface shortwave downward irradiance was in the range of 2.46–7.49 $KWh/m^2/day$ (102.5–312.1 W/m^2). Thus, in our process, the average continual radiation was in the range of 0.43–1.32 W, and the degradation rates can be summarized in Figure 9. In this case, in the presence of the photocatalysts, TC25 and TC50 MO rapidly becomes degraded, as the rate increases to 96.0% and 90.2% for the first 30 min of irradiation (Figures S9 and S10). It must be pointed out that control experiments performed under the conditions of irradiation in the absence of the photocatalyst did not show any change in the azo-dye solution absorbance. It can also be noted that under similar reaction conditions, a lower degradation rate (similar to TC75) was obtained with a commercially available gold catalyst, supported by TiO_2 (TAu).

The results demonstrate that in all cases, the photocatalytic performance of the composite materials strongly depends on the C-dots percentage in TiO_2. A remarkable photocatalytic result in the case of low to moderate C-dot loading turns to reduced activity when the C-dot loading increases in the TiO_2 core. This could be attributed to the excess of C-dots on the surface of TiO_2 in TC75, which cause blockage of the pore channels, thus hindering light-harvesting and charge transfer [23,64].
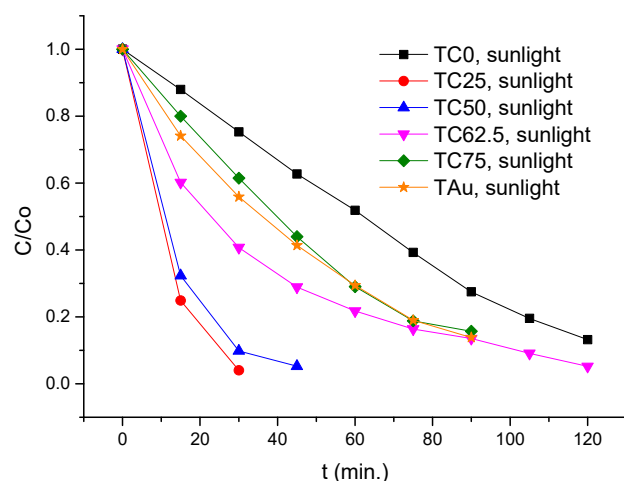
Figure 9. MO degradation rates in the presence of TAu and TC0–75 photocatalysts under sunlight irradiation.

Based on the heterogeneity of the catalytic system, the TC catalysts can be easily separated from the reaction mixture by careful decantation of the aqueous solution or, more accurately, via centrifugation, followed by washing with water and ethanol. Thus, the stability of the TC50 catalyst was examined by performing ten consecutive catalytic tests by irradiating 5 ppm of MO in the presence of 0.2% *w/v* photocatalyst for 180 min under simulated solar light. As it can be seen in Figure 10, even after 10 cycles, 89.3% of MO was degraded within 180 min, leading to complete degradation after 360 min in the 10th cycle. The UV-Vis spectra and macroscopic evaluation before and after ten consecutive cycles of MO degradation using TC50 under visible light are illustrated in Figures S11 and S12. To the best of our knowledge, this result is far superior compared to already published works on TiO_2/C-dots [23,25], showing a robust, almost eternal photocatalytic system for continuous pollution protection.
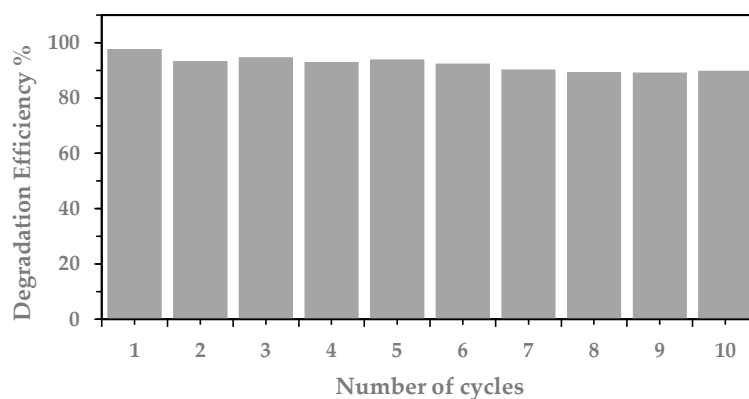

Figure 10. Reusability of TC50 photocatalyst in the MO degradation under simulated solar irradiation.

Since the photodegradation of MO in the presence of TiO_2/Cdots follows a pseudo-first-order kinetic model, photocatalytic efficiency of all TC25–75 nanocomposites, compared to TC0 and TAu, under different radiation sources can be summarized in Table 1. In all cases, the rate constants were obtained by plotting $\ln(C_0/C)$ to irradiation time. As it can be seen, the degradation rate of MO for TC25 and TC50 under visible light irradiation is 12.5 times higher than that of pure TiO_2 (TC0), while under UV-A and solar light irradiation, a 3.4–4.6 and 4.4–5.7 times higher rate was observed. Moreover, upon solar light irradiation, TC25 and TC50 provided a 3.3–4.3 higher degradation rate compared to commercially available Au/TiO_2 (TAu) catalyst.

Table 1. Comparison of photocatalytic efficiency between TC0–75 and TAu using the first order fitting kinetic data of MO degradation under different radiation sources.

Type of Irradiation	Photocatalyst	K_{app} (min^{-1})	R^2	Degradation Rate (%)/min
UV-A light	TC0	1.10×10^{-2}	0.997	45.4/60
	TC25	5.07×10^{-2}	0.982	96.2/60
	TC50	3.79×10^{-2}	0.997	90.9/60
	TC62.5	1.72×10^{-2}	0.999	62.9/60
	TC75	1.21×10^{-2}	0.991	46.1/60
Visible light	TC0	0.18×10^{-2}	0.984	20.8/120
	TC25	2.28×10^{-2}	0.991	91.4/120
	TC50	2.29×10^{-2}	0.991	92.0/120
	TC62.5	0.74×10^{-2}	0.998	56.9/120
	TC75	0.49×10^{-2}	0.980	48.7/120
Solar light	TC0	1.59×10^{-2}	0.971	48.1/60
	TC25	9.13×10^{-2}	0.983	96.0/30
	TC50	6.96×10^{-2}	0.992	90.2/30
	TC62.5	2.41×10^{-2}	0.994	78.2/60
	TC75	2.06×10^{-2}	0.993	71.0/60
	TAu	2.14×10^{-2}	0.998	70.6/60

3.3. Photocatalytic Activity of Multifunctional Protective Films

The photocatalytic ability of the catalysts was also tested after their incorporation into the silica-based consolidant FX-C and their application onto cementitious mortars. Mixtures containing 4% *w/w* of TC0, TC25 and TAu into the FX-C were prepared (Figure S1) and brushed until saturation onto the surface of the cementitious specimens, which were previously cleaned with isopropanol. TC25 was selected on the grounds of its bests photocatalytic activity both under solar and UV irradiation, as it was proved in the experiments with the MO degradation. For comparison, a part of the surface of the samples was left untreated, and another one was brushed with the consolidant without a catalyst. In order to explore the most favorable application method, another testing surface was created by first applying a layer of the FX-C until saturation and, afterward, a layer of the mixture of the consolidant with TC25.

In order to study the self-cleaning properties of the specimens with the different protective films, two drops (around 0.025 mL each) of methylene blue (MB) were released on each coating, and its degradation was evaluated by comparing the color difference of the stained surface with the color of the surface before the MB application (Figure S2), using a spectrophotometer. The goal is to observe a decline in this color difference (ΔE), reaching, in the best case, a value below 5. The macroscopic evaluation of MB degradation on treated and untreated cement mortars is reported in Figure S2. The specimens were tested under UV-A and visible light irradiation for 48 h, and the results do not significantly differ regarding the type of radiation used. As shown in Figure 11 and Table 2, the protective films containing TC0 and TAu were those with the best performance, reaching the desired value within 48 h.

In addition to the above-mentioned photocatalysts, the surface treated with a double layer consisting of FX-C and FX-C/TC25 also demonstrated considerable self-cleaning properties both under UV-A and visible light irradiation, reaching a value of 7.21 and 5.76, respectively. Moreover, in the case of the protective films containing TC25, the degradation of the pigment was also notable after 48 h of irradiation. The untreated surfaces and the surface treated with solely FX-C showed an insignificant decline in the color difference that can be attributed to the degradation of the dye because of the action of the irradiation. It should be mentioned that, despite the fact that the FX-C/TAu film demonstrated substantial photocatalytic properties, it cannot be proposed as a viable

protective option for monumental surfaces, as it changes the color of the surface radically after its application (Figure S2).
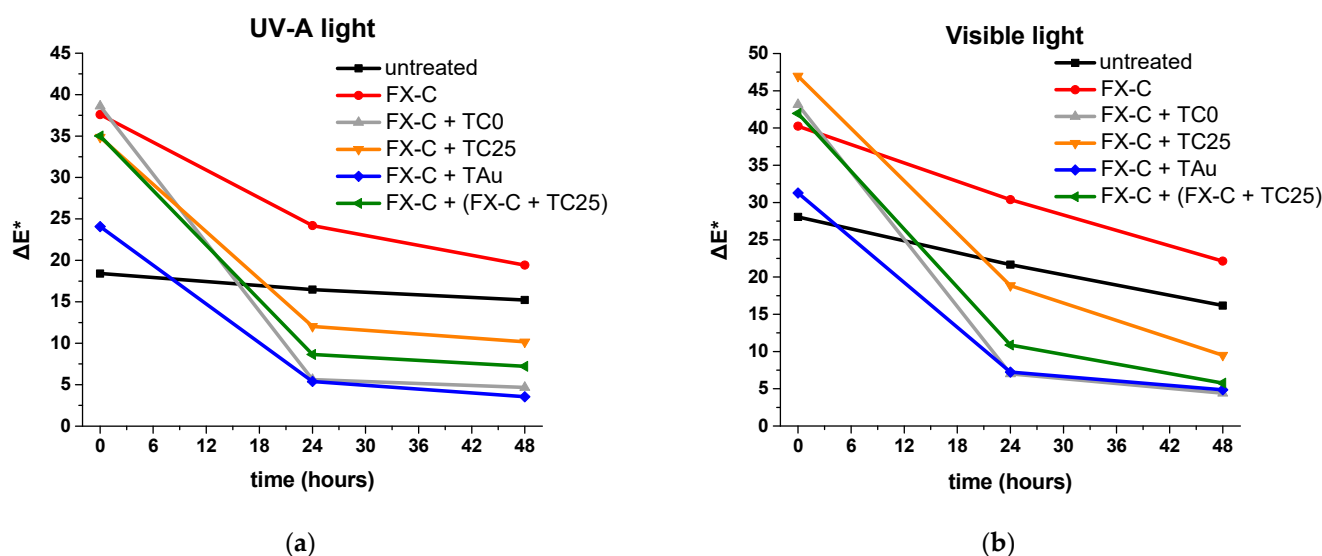

(**a**)

(**b**)

Figure 11. Variation graphs of the specimens' color difference (ΔE^*) as a function of time for MB degradation under (**a**) UV-A and (**b**) simulated solar light irradiation.

Table 2. Comparison of the specimens' color difference (ΔE^*) as a function of time for MB degradation under different radiation sources.

Light Irradiation	Time (h)	ΔE^*					
		Untreated	FX-C	FX-C + TC0	FX-C + TC25	FX-C + TAu	FX-C + (FX-C + TC25)
UV-A light	0	18.41	37.60	38.62	34.88	24.08	35.02
	24	16.48	24.20	5.62	12.04	5.39	8.64
	48	15.21	19.43	4.67	10.16	3.54	7.21
Visible light	0	28.07	40.24	43.14	46.97	31.28	41.95
	24	21.67	30.39	7.00	18.85	7.24	10.88
	48	16.17	22.14	4.40	9.50	4.87	5.77

These in situ experiments clearly pointed out that significant differences arose in the efficiency of the pure photocatalysts and the subsequent incorporation within protective coatings [65,66]. Regardless of the best performed TC25 and TC50 photocatalysts compared to TC0 and TAu under UV-A and solar irradiation, however, the nanocomposites that faster degraded the MB resulted in being those without C-dot loading into TiO_2. Therefore, self-cleaning coatings applied to building materials require individual experiments, including a treatment process with both protective and self-cleaning agents. It was demonstrated that for cementitious surfaces, FX-C with pure TiO_2 and a double layer treatment of FX-C along with FX-C + TC25 could be considered promising solutions against pollutant decay. This study highlighted the need for in situ testing of the nanostructured protective coatings, in which the well-established photocatalysts were integrated for multifunctional building protection.

4. Conclusions

TiO_2/C-dots composites with different C-dot loading were synthesized using citric acid, hydroxylamine and titanium isopropoxide (TTIP) by a facile, green and large-scale hydrothermal strategy. The different mass ratios of C-dots solution to TTIP produced TiO_2

functionalized photocatalysts that were characterized by the anatase structure, formed at a low calcination temperature of 200 °C. The C-dot modified TiO_2 showed efficient photocatalytic MO and MB degradation activity under UV-A and, more specifically, under visible light and sunlight radiation. Under UV-A, visible and solar light irradiation, the degradation rate of MO for TC25 and TC50 is 3.4–12.5 times higher compared to pure TiO_2 (TC0), while solar light provides a 3.3–4.3 higher degradation rate of MO for TC25 and TC50 than commercially available Au/TiO_2 (TAu) catalyst. Additionally, the photocatalysts can be recycled at least 10 times without losing their activity, showing the potentiality of these nanocomposites for continuous pollution protection. Finally, it was demonstrated that the application of multifunctional coatings on the cementitious matrix played a significant role. In the in situ applications of the self-cleaning coatings onto cementitious materials, the protective film of the silica-based FX-C with the pure TiO_2 and the double layer treatment with FX-C and FX-C + TC25 resulted in being the best-performing coatings against pollutant degradation.

Supplementary Materials: The following supporting information can be downloaded at: https://www.mdpi.com/article/10.3390/coatings12050587/s1, Table S1: Mix design of cement mortars treated with the nanocomposites of FX-C with catalysts; Figure S1: Sols of FX-C and nanocomposites of FX-C with catalysts; Figure S2: Macroscopical evaluation of the gradual MB degradation on treated and untreated cement mortars, before and after MB application, under (a) UV-A and (b) visible irradiation; Figure S3: (a,b) TEM images and (c) diameter distribution histogram of C-dots; Figure S4: (a) TEM image and (b) diameter distribution histogram of TC75; Figure S5: UV-Vis spectra of gradual MO degradation using TC50 upon UV-A irradiation; Figure S6: Macroscopic image of gradual MO degradation using TC50 upon UV-A irradiation; Figure S7: UV-Vis spectra of gradual MO degradation using TC50 upon simulated solar light irradiation; Figure S8: Macroscopic image of gradual MO degradation using TC50 upon simulated solar light irradiation; Figure S9: UV-Vis spectra of gradual MO degradation using TC50 under sunlight irradiation; Figure S10: Macroscopic image of gradual MO degradation using TC50 under sunlight irradiation; Figure S11: UV-Vis spectra before (0 min) and after ten consecutive cycles (1–10) of MO degradation using TC50 upon simulated solar light irradiation; Figure S12: Macroscopic image before (0 min) and after ten consecutive cycles (1–10) of MO degradation using TC50 upon simulated solar light irradiation.

References

1. GBD 2016 Risk Factors Collaborators. Global, regional, and national comparative risk assessment of 84 behavioural, environmental and occupational, and metabolic risks or clusters of risks, 1990–2016: A systematic analysis for the Global Burden of Disease Study 2016. *Lancet* **2017**, *390*, 1345–1422. [CrossRef]
2. Masson-Delmotte, V.; Zhai, P.; Pirani, A.; Connors, S.L.; Péan, C.; Berger, S.; Caud, N.; Chen, Y.; Goldfarb, L.; Gomis, M.I.; et al. (Eds.) *IPCC, 2021: Climate Change 2021: The Physical Science Basis. Contribution of Working Group I to the Sixth Assessment Report of the Intergovernmental Panel on Climate Change*; Cambridge University Press: Cambridge, UK, 2021; Available online: https://www.ipcc.ch/report/ar6/wg1/#FullReport (accessed on 27 February 2022).
3. Vandyck, T.; Keramidas, K.; Kitous, A.; Spadaro, J.V.; Van Dingenen, R.; Holland, M.; Saveyn, B. Air quality co-benefits for human health and agriculture counterbalance costs to meet Paris Agreement pledges. *Nat. Commun.* **2018**, *9*, 4939. [CrossRef] [PubMed]
4. Kapridaki, C.; Pinho, L.; Mosquera, M.J.; Maravelaki-Kalaitzaki, P. Producing photoactive, transparent and hydrophobic SiO_2-crystalline TiO_2 nanocomposites at ambient conditions with application as self-cleaning coatings. *Appl. Catal. B Environ.* **2014**, *156–157*, 416–427. [CrossRef]
5. Ganesh, V.A.; Raut, H.K.; Nair, A.S.; Ramakrishna, S. A review on self-cleaning coatings. *J. Mater. Chem.* **2011**, *21*, 16304–16322. [CrossRef]
6. Sakar, M.; Prakash, R.M.; Do, T.-O. Insights into the TiO_2-Based Photocatalytic Systems and Their Mechanisms. *Catalysts* **2019**, *9*, 680. [CrossRef]
7. Fujishima, A.; Honda, K. Electrochemical photolysis of water at a semiconductor electrode. *Nature* **1972**, *238*, 37–38. [CrossRef] [PubMed]
8. Schneider, J.; Matsuoka, M.; Takeuchi, M.; Zhang, J.; Horiuchi, Y.; Anpo, M.; Bahnemann, D.W. Understanding TiO_2 Photocatalysis: Mechanisms and Materials. *Chem. Rev.* **2014**, *114*, 9919–9986. [CrossRef]
9. Linsebigler, A.L.; Lu, G.; Yates, J.T. Photocatalysis on TiO_2 Surfaces: Principles, Mechanisms, and Selected Results. *Chem. Rev.* **1995**, *95*, 735–758. [CrossRef]
10. Oseghe, E.O.; Msagati, T.A.M.; Mamba, B.B.; Ofomaja, A.E. An efficient and stable narrow bandgap carbon dot-brookite composite over other CD-TiO_2 polymorphs in rhodamine B degradation under LED light. *Ceram. Int.* **2019**, *45*, 14173–14181. [CrossRef]
11. Zhang, J.; Zhou, P.; Liu, J.; Yu, J. New understanding of the difference of photocatalytic activity among anatase, rutile and brookite TiO_2. *Phys. Chem. Chem. Phys.* **2014**, *16*, 20382–20386. [CrossRef] [PubMed]
12. Xu, X.; Ray, R.; Gu, Y.; Ploehn, H.J.; Gearheart, L.; Raker, K.; Scrivens, W.A. Electrophoretic Analysis and Purification of Fluorescent Single-Walled Carbon Nanotube Fragments. *J. Am. Chem. Soc.* **2004**, *126*, 12736–12737. [CrossRef] [PubMed]
13. Liu, J.; Li, R.; Yang, B. Carbon Dots: A New Type of Carbon-Based Nanomaterial with Wide Applications. *ACS Cent. Sci.* **2020**, *6*, 2179–2195. [CrossRef]
14. Lim, S.Y.; Shen, W.; Gao, Z. Carbon quantum dots and their applications. *Chem. Soc. Rev.* **2015**, *44*, 362–381. [CrossRef]
15. Li, H.; He, X.; Kang, Z.; Huang, H.; Liu, Y.; Liu, J.; Lian, S.; Tsang, C.H.A.; Yang, X.; Lee, S.-T. Water-Soluble Fluorescent Carbon Quantum Dots and Photocatalyst Design. *Angew. Chem. Int. Ed.* **2010**, *49*, 4430–4434. [CrossRef]
16. Hazarika, D.; Karak, N. Photocatalytic degradation of organic contaminants under solar light using carbon dot/titanium dioxide nanohybrid, obtained through a facile approach. *Appl. Surf. Sci.* **2016**, *376*, 276–285. [CrossRef]
17. Chen, J.; Shu, J.; Anqi, Z.; Juyuan, H.; Yan, Z.; Chen, J. Synthesis of carbon quantum dots/TiO_2 nanocomposite for photo-degradation of Rhodamine B and cefradine. *Diam. Relat. Mater.* **2016**, *70*, 137–144. [CrossRef]
18. Miao, R.; Luo, Z.; Zhong, W.; Chen, S.-Y.; Jiang, T.; Dutta, B.; Nasr, Y.; Zhang, Y.; Suib, S.L. Mesoporous TiO_2 modified with carbon quantum dots as a high-performance visible light photocatalyst. *Appl. Catal. B Environ.* **2016**, *189*, 26–38. [CrossRef]
19. Syafei, D.; Sugiarti, S.; Darmawan, N.; Khotib, M. Synthesis of TiO_2/Carbon Nanoparticle (C-dot) Composites as Active Catalysts for Photodegradation of Persistent Organic Pollutant. *Indones. J. Chem.* **2017**, *17*, 37–42. [CrossRef]
20. Wongso, V.; Chung, H.K.; Sambudi, N.S.; Sufian, S.; Abdullah, B.; Wirzal, M.D.H.; Ang, W.L. Silica–carbon quantum dots decorated titanium dioxide as sunlight-driven photocatalyst to diminish acetaminophen from aquatic environment. *J. Photochem. Photobiol. A Chem.* **2020**, *394*, 112436. [CrossRef]
21. Li, F.; Tian, F.; Liu, C.; Wang, Z.; Du, Z.; Li, R.; Zhang, L. One-step synthesis of nanohybrid carbon dots and TiO_2 composites with enhanced ultraviolet light active photocatalysis. *RSC Adv.* **2015**, *5*, 8389–8396. [CrossRef]
22. Kumar, M.S.; Yasoda, K.H.; Kumaresan, D.; Kothurkar, N.K.; Batabyal, S.K. TiO_2-carbon quantum dots (CQD) nanohybrid: Enhanced photocatalytic activity. *Mater. Res. Express* **2018**, *5*, 075502. [CrossRef]
23. Deng, Y.; Chen, M.; Chen, G.; Zou, W.; Zhao, Y.; Zhang, H.; Zhao, Q. Visible−Ultraviolet Upconversion Carbon Quantum Dots for Enhancement of the Photocatalytic Activity of Titanium Dioxide. *ACS Omega* **2021**, *6*, 4247–4254. [CrossRef] [PubMed]
24. Luo, H.; Dimitrov, S.; Daboczi, M.; Kim, J.-S.; Guo, Q.; Fang, Y.; Stoeckel, M.-A.; Samorì, P.; Fenwick, O.; Sobrido, A.B.J.; et al. Nitrogen-Doped Carbon Dots/TiO_2 Nanoparticle Composites for Photoelectrochemical Water Oxidation. *ACS Appl. Nano Mater.* **2020**, *3*, 3371–3381. [CrossRef]
25. Wang, A.; Xiao, X.; Zhou, C.; Lyu, F.; Fu, L.; Wang, C.; Ruan, S. Large-scale synthesis of carbon dots/TiO_2 nanocomposites for the photocatalytic color switching system. *Nanoscale Adv.* **2019**, *1*, 1819–1825. [CrossRef]
26. Stefanakis, D.; Krasoudaki, T.; Kaditis, A.-I.; Bakolas, A.; Maravelaki, P.-N. Design of Novel Photocatalytic Films for the Protection of Architectural Surfaces via the Incorporation of Green Photocatalysts. *Coatings* **2021**, *11*, 934. [CrossRef]

27. Barberena-Fernández, A.M.; Carmona-Quiroga, P.M.; Blanco-Varela, M.T. Interaction of TEOS with cementitious materials: Chemical and physical effects. *Cem. Concr. Compos.* **2015**, *55*, 145–152. [CrossRef]

28. Al-Qaradawi, S.; Salman, S.R. Photocatalytic degradation of methyl orange as a model compound. *J. Photochem. Photobiol. A Chem.* **2002**, *148*, 161–168. [CrossRef]

29. Kapetanaki, K.; Vazgiouraki, E.; Stefanakis, D.; Fotiou, A.; Anyfantis, G.C.; García-Lodeiro, I.; Blanco-Varela, M.T.; Arabatzis, I.; Maravelaki, P.N. TEOS Modified With Nano-Calcium Oxalate and PDMS to Protect Concrete Based Cultural Heritage Buildings. *Front. Mater.* **2020**, *7*, 16. [CrossRef]

30. Maravelaki, P.N.; Kapetanaki, K.; Stefanakis, D. TEOS-PDMS-Calcium Oxalate Hydrophobic Nanocomposite for Protection and Stone Consolidation. *Heritage* **2021**, *4*, 4068–4075. [CrossRef]

31. David, M.E.; Ion, R.-M.; Grigorescu, R.M.; Iancu, L.; Andrei, E.R. Nanomaterials used in conservation and restoration of cultural heritage: An up-to-date overview. *Materials* **2020**, *13*, 2064. [CrossRef] [PubMed]

32. Enesca, A.; Andronic, L.; Duta, A. The influence of surfactants on the crystalline structure, electrical and photocatalytic properties of hybrid multi-structured (SnO_2, TiO_2 and WO_3) thin films. *Appl. Surf. Sci.* **2012**, *258*, 4339–4346. [CrossRef]

33. Xu, H.; Hao, Z.; Feng, W.; Wang, T.; Fu, X. The floating photocatalytic spheres loaded with weak light-driven TiO_2-based catalysts for photodegrading tetracycline in seawater. *Mater. Sci. Semicond. Process* **2022**, *144*, 106610. [CrossRef]

34. Mugundan, S.; Praveen, P.; Sridhar, S.; Prabu, S.; Mary, K.L.; Ubaidullah, M.; Shaikh, S.F.; Kanagesan, S. Sol-gel synthesized barium doped TiO_2 nanoparticles for solar photocatalytic application. *Inorg. Chem. Commun.* **2022**, *139*, 109340. [CrossRef]

35. Rosales, A.; Esquivel, K. SiO_2@TiO_2 Composite Synthesis and Its Hydrophobic Applications: A Review. *Catalysts* **2020**, *10*, 171. [CrossRef]

36. Rosales, A.; Maury-Ramírez, A.; Mejía-De Gutiérrez, R.; Guzmán, C.; Esquivel, K. SiO_2@TiO_2 Coating: Synthesis, Physical Characterization and Photocatalytic Evaluation. *Coatings* **2018**, *8*, 120. [CrossRef]

37. Franzoni, E.; Fregni, A.; Gabrielli, R.; Graziani, G.; Sassoni, E. Compatibility of photocatalytic TiO_2-based finishing for renders in architectural restoration: A preliminary study. *Build. Environ.* **2014**, *80*, 125–135. [CrossRef]

38. Rosales, A.; Ortiz-Frade, L.; Medina-Ramirez, I.E.; Godínez, L.A.; Esquivel, K. Self-cleaning of SiO_2-TiO_2 coating: Effect of sonochemical synthetic parameters on the morphological, mechanical, and photocatalytic properties of the films. *Ultrason. Sonochem.* **2021**, *73*, 105483. [CrossRef] [PubMed]

39. Maravelaki-Kalaitzaki, P.; Agioutantis, Z.; Lionakis, E.; Stavroulaki, M.; Perdikatsis, V. Physico-chemical and mechanical characterization of hydraulic mortars containing nano-titania for restoration applications. *Cem. Concr. Compos.* **2013**, *36*, 33–41. [CrossRef]

40. Balliana, E.; Ricci, G.; Pesce, C.; Zendri, E. Assessing the value of green conservation for cultural heritage: Positive and critical aspects of already available methodologies. *Int. J. Conserv. Sci.* **2016**, *7*, 185–202. Available online: https://ijcs.ro/public/IJCS-16-SI01_Balliana.pdf (accessed on 14 October 2021).

41. Petronella, F.; Pagliarulo, A.; Truppi, A.; Lettieri, M.; Masieri, M.; Calia, A.; Curri, M.L.; Comparelli, R. TiO_2 Nanocrystal Based Coatings for the Protection of Architectural Stone: The Effect of Solvents in the Spray-Coating Application for a Self-Cleaning Surfaces. *Coatings* **2018**, *8*, 356. [CrossRef]

42. Kapridaki, C.; Maravelaki-Kalaitzaki, P. TiO_2–SiO_2–PDMS nano-composite hydrophobic coating with self-cleaning properties for marble protection. *Prog. Org. Coat.* **2013**, *76*, 400–410. [CrossRef]

43. Kapridaki, C.; Verganelaki, A.; Dimitriadou, P.; Maravelaki-Kalaitzaki, P. Conservation of Monuments by a Three-Layered Compatible Treatment of TEOS-Nano-Calcium Oxalate Consolidant and TEOS-PDMS-TiO_2 Hydrophobic/Photoactive Hybrid Nanomaterials. *Materials* **2018**, *11*, 684. [CrossRef]

44. Stefanakis, D.; Philippidis, A.; Sygellou, L.; Filippidis, G.; Ghanotakis, D.; Anglos, D. Synthesis of fluorescent carbon dots by a microwave heating process: Structural characterization and cell imaging applications. *J. Nanopart. Res.* **2014**, *16*, 12646. [CrossRef]

45. De Muynck, W.; Ramirez, A.M.; De Belie, N.; Verstraete, W. Evaluation of strategies to prevent algal fouling on white architectural and cellular concrete. *Int. Biodeterior. Biodegrad.* **2009**, *63*, 679–689. [CrossRef]

46. Allena, N.S.; Mahdjoubd, N.; Vishnyakovb, V.; Kellyb, P.J.; Kriekc, R.J. The effect of crystalline phase (anatase, brookite and rutile) and size on the photocatalytic activity of calcined polymorphic titanium dioxide (TiO_2). *Polym. Degrad. Stab.* **2018**, *150*, 31–36. [CrossRef]

47. Patterson, A.L. The Scherrer Formula for X-ray Particle Size Determination. *Phys. Rev.* **1939**, *56*, 978. [CrossRef]

48. Shah, A.H.; Rather, M.A. Effect of calcination temperature on the crystallite size, particle size and zeta potential of TiO_2 nanoparticles synthesized via polyol-mediated method. *Mater. Today Proc.* **2021**, *44*, 482–488. [CrossRef]

49. Esquivel, K.; Nava, R.; Zamudio-Méndez, A.; González, M.V.; Jaime-Acuña, O.E.; Escobar-Alarcón, L.; Peralta-Hernández, J.M.; Pawelec, B.; Fierro, J.L.G. Microwave-assisted synthesis of (S)Fe/TiO_2 systems: Effects of synthesis conditions and dopant concentration on photoactivity. *Appl. Catal. B Environ.* **2013**, *140–141*, 213–224. [CrossRef]

50. Górska, P.; Zaleska, A.; Kowalska, E.; Klimczuk, T.; Sobczak, J.W.; Skwarek, E.; Janusz, W.; Hupka, J. TiO_2 photoactivity in vis and UV light: The influence of calcination temperature and surface properties. *Appl. Catal. B Environ.* **2008**, *84*, 440–447. [CrossRef]

51. Zhang, H.; Banfield, J.F. Thermodynamic analysis of phase stability of nanocrystalline titania. *J. Mater. Chem.* **1998**, *8*, 2073–2076. [CrossRef]

52. Kibasomba, P.M.; Dhlamini, S.; Maaza, M.; Liu, C.-P.; Rashad, M.M.; Rayan, D.A.; Mwakikunga, B.W. Strain and grain size of TiO$_2$ nanoparticles from TEM, Raman spectroscopy and XRD: The revisiting of the Williamson-Hall plot method. *Results Phys.* **2018**, *9*, 628–635. [CrossRef]

53. Munafò, P.; Quagliarini, E.; Goffredo, G.B.; Bondioli, F.; Licciulli, A. Durability of nano-engineered TiO$_2$ self-cleaning treatments on limestone. *Constr. Build. Mater.* **2014**, *65*, 218–231. [CrossRef]

54. Zamudio-Méndez, A.; Sánchez-Palma, E.; Navarro-López, R.; Pérez-Lara, M.A.; Rivera Muñoz, E.M.; Godínez, L.A.; Velázquez-Castillo, R.; Nava, R.; Esquivel, K. Self-Cleaning Activity on Concrete Surfaces Coated with Fe- and S-Doped TiO$_2$ Synthesized by Sol–Gel Microwave Method. *J. Nanosci. Nanotechnol.* **2017**, *17*, 5637–5645. [CrossRef]

55. Shetty, R.; Chavan, V.B.; Kulkarni, P.S.; Kulkarni, B.D.; Kamble, S.P. Photocatalytic Degradation of Pharmaceuticals Pollutants Using N-Doped TiO$_2$ Photocatalyst: Identification of CFX Degradation Intermediates. *Indian Chem. Eng.* **2017**, *59*, 177–199. [CrossRef]

56. Wu, W.-Y.; Chang, Y.-M.; Ting, J.-M. Room-temperature synthesis of single-crystalline anatase TiO$_2$ nanowires. *Cryst. Growth Des.* **2010**, *10*, 1646–1651. [CrossRef]

57. Lu, W.; Qin, X.; Liu, S.; Chang, G.; Zhang, Y.; Luo, Y.; Asiri, A.M.; Al-Youbi, A.O.; Sun, X. Economical, green synthesis of fluorescent carbon nanoparticles and their use as probes for sensitive and selective detection of mercury(II) ions. *Anal. Chem.* **2012**, *84*, 5351–5357. [CrossRef] [PubMed]

58. Nie, X.; Jiang, C.; Wu, S.; Chen, W.; Lv, P.; Wang, Q.; Liu, J.; Narh, C.; Cao, X.; Ghiladi, R.A.; et al. Carbon quantum dots: A bright future as photosensitizers for in vitro antibacterial photodynamic inactivation. *J. Photochem. Photobiol. B Biol.* **2020**, *206*, 111864. [CrossRef]

59. Tauc, J. Optical properties of amorphous semiconductors. In *Amorphous and Liquid Semiconductors*; Tauc, J., Ed.; Springer: Boston, MA, USA, 1974; pp. 159–220. [CrossRef]

60. Kubelka, P. New contributions to the optics of intensely light-scattering materials. Part I. *J. Opt. Soc. Am.* **1948**, *38*, 448–457. [CrossRef]

61. Wang, J.; Guo, B.; Zhang, X.; Zhang, Z.; Han, J.; Wu, J. Sonocatalytic degradation of methyl orange in the presence of TiO$_2$ catalysts and catalytic activity comparison of rutile and anatase. *Ultrason. Sonochem.* **2005**, *12*, 331–337. [CrossRef] [PubMed]

62. Priyanshu, V.; Sujoy, K.S. Degradation kinetics of pollutants present in a simulated wastewater matrix using UV/TiO$_2$ photocatalysis and its microbiological toxicity assessment. *Res. Chem. Intermed.* **2017**, *43*, 6317–6341. [CrossRef]

63. NASA's Power Data Access Viewer. Available online: https://power.larc.nasa.gov/data-access-viewer/ (accessed on 18 February 2022).

64. Ke, J.; Li, X.; Zhao, Q.; Liu, B.; Liu, S.; Wang, S. Upconversion carbon quantum dots as visible light responsive component for efficient enhancement of photocatalytic performance. *J. Colloid Interface Sci.* **2017**, *496*, 425–433. [CrossRef] [PubMed]

65. Gherardi, F. Current and future trends in protective treatments for stone heritage. In *Conserving Stone Heritage*; Gherardi, F., Maravelaki, P.N., Eds.; Springer: Cham., Switzerland, 2022; pp. 137–176. [CrossRef]

66. Falchi, L.; Zendri, E.; Müller, U.; Fontana, P. The influence of water-repellent admixtures on the behaviour and the effectiveness of Portland limestone cement mortars. *Cem. Concr. Compos.* **2015**, *59*, 107–118. [CrossRef]